Northumbria Research Link

UniversityLibrary

REGULAR PAPER

CrossMark

Enhanced external quantum efficiency from Cu₂ZnSn(S,Se)₄ solar cells prepared from nanoparticle inks

Yongtao Qu[1], Guillaume Zoppi[1], Laurence M. Peter[2], Sophie Jourdain[1], and Neil S. Beattie[1*]

[1]Department of Mathematics, Physics and Electrical Engineering, Northumbria University, Newcastle upon Tyne NE1 8ST, U.K.
[2]Department of Chemistry, University of Bath, Bath BA2 7AY, U.K.

*E-mail: neil.beattie@northumbria.ac.uk

Cu₂ZnSn(S,Se)₄ (CZTSSe) thin film photovoltaic absorber layers are fabricated by selenizing Cu₂ZnSnS₄ (CZTS) nanoparticle thin films in a selenium rich atmosphere. The selenium vapor pressure is controlled to optimize the morphology and quality of the CZTSSe thin film. The largest grains are formed at the highest selenium vapor pressure of 226 mbar. Integrating this photovoltaic absorber layer in a conventional thin film solar cell structure yields a champion short circuit current of 37.9 mA/cm² without an antireflection coating. This stems from an improved external quantum efficiency characteristic in the visible and near-infrared part of the solar spectrum. The physical basis of this improvement is qualitatively attributed to a substantial increase in the minority carrier diffusion length. © 2018 The Japan Society of Applied Physics

1. Introduction

With the advantage of a direct energy band gap (0.9–1.5 eV),[1] high absorption coefficient ($>10^4$ cm^{-1} in the visible region) and potential low-cost production, Cu₂ZnSn(S,Se)₄ (CZTSSe) is a promising thin film photovoltaic (PV) material experiencing rapid progress in recent years.[2] Among the variety of techniques employed for preparation of the absorber films,[3–9] kesterite PV has so far demonstrated a 12.6% record efficiency using a hydrazine-solution based method.[10] However, the selenization of Cu₂ZnSnS₄ (CZTS) nanoparticle inks currently provides the only approach that allows phase formation prior to the film deposition.[11,12] Recently, a CZTSSe solar cell (with an antireflective coating) fabricated from a CZTS nanoparticle ink has been reported with a solar energy conversion efficiency of 9.3%.[13] This progress was attributed to careful control of the nanoparticle synthesis. In addition to the nanoparticle ink however, the selenization process plays a key role in the fabrication of high quality CZTSSe thin film PV absorber layers, where CZTS nanoparticles are converted into large CZTSSe grains and the number of grain boundaries is minimized.[14,15] We have recently investigated the kinetics of the selenization process and found that these have a fundamental influence on the quality of the resulting CZTSSe thin film and consequently the PV device performance.[16]

In this work we apply this insight to optimize the CZTSSe grain growth process for a thin film PV absorber prepared from a CZTS nanoparticle ink. The results indicate that the CZTSSe absorber layer morphology and crystal quality are strongly influenced by the selenium vapor pressure and play important roles in determining the performance of devices made from these absorbers. Significantly, the highest selenium vapor pressure results in a relatively large-grain CZTSSe photovoltaic absorber which, when integrated within a thin film solar cell exhibits a near-ideal external quantum efficiency. In turn this leads to superior values of short circuit current density.

2. Experimental methods

CZTS nanoparticles used in this study were produced by injection of metallic precursors into a hot surfactant.[17] The resulting nanoparticle inks were deposited on Mo-glass substrates via spin-coating.[18] To induce grain growth, CZTS nanoparticle thin films were selenized in a tube furnace. The as-deposited precursor thin films were placed inside a cylindrical graphite box with selenium pellets placed directly beneath the substrate. The furnace was evacuated (6.0×10^{-3} mbar) and an argon atmosphere (~10 mbar) was provided before the temperature was increased (~20 °C/min) to 500 °C. This temperature was then held for 20 min before being cooled down rapidly (~20 °C/min) as detailed elsewhere.[16]

As the graphite box was only partially closed, the selenium partial pressure inside was not constant during the ramp up stage. Upon heating, selenium evaporates and escapes into quartz tube until equilibrium is reached. The equilibrium selenium vapor pressure can be estimated using the model developed by Scragg.[19] The fraction (F) of selenium molecules that remains inside the box after equilibration is given by

$$F = \frac{P_{Ar} + P_{Se_2} V_b/V_t}{P_{Ar} + P_{Se_2}}, \quad (1)$$

where P_{Ar} is the initial background pressure of argon, V_b is the volume of the graphite box (3.0×10^{-5} m³), and V_t is the total volume of the quartz tube (9.4×10^{-4} m³). $P_{Se_2} = n_{Se_2} RT/V_b$ is the pressure of selenium that can be achieved within the box if the box was kept sealed, where n_{Se_2} is the total number moles formed from the evaporation of the Se pellets, R is the ideal gas constant and T is the absolute temperature. The partial pressure of selenium P_{e,Se_2} within the graphite box after pressure equilibration can therefore be given as

$$P_{e,Se_2} = P_{Se_2} F. \quad (2)$$

Based on Eq. (2), the selenium equilibrium vapor pressure was determined to be 31, 53, 75, 140, and 226 mbar by inserting 50, 100, 150, 300, and 500 mg of selenium in the graphite box respectively.

The resulting CZTSSe thin films were integrated in solar cell devices with a configuration of Mo/CZTSSe/CdS/ i-ZnO/ITO/Ni–Al, where "i" stands for intrinsic and ITO is indium tin oxide. The CdS buffer layer was deposited using a chemical bath process.[18] After the CdS deposition, the samples were rinsed with deionized water, dried under a

nitrogen stream and then annealed at 200 °C for 10 min in air. The transparent oxide layer, i-ZnO and ITO were deposited by magnetron sputtering. Finally, the front contact grid was deposited by electron beam evaporation of Ni (~50 nm) and Al (~1 μm) through a shadow mask. Each solar cell was defined by scribing the substrate into nine 0.16 cm^2 devices.

The thin film morphology after selenization was determined using a Tescan Mira 3 scanning electron microscope (SEM). The structure of the CZTSSe thin films was examined using X-ray diffraction (XRD) carried out with a Siemens D-5000 diffractometer using an Ni-filtered Cu Kα radiation source. Elemental depth profiling was performed by secondary ion mass spectroscopy (SIMS) using a primary Ar$^+$ beam of 4 keV, a crater area of $500 \times 500 \, \mu m^2$ and a gating of 10%. The external quantum efficiency (EQE) measurements were performed using a double grating monochromator (Bentham Instruments M300) with illumination normalized against calibrated silicon and germanium detectors. Current density versus voltage (J–V) measurements were performed in a four-point probe configuration using a Keithley 2400 series sourcemeter. Samples were illuminated with an Abet Technologies Sun 2000 solar simulator with an air mass (AM) 1.5 spectrum adjusted to 100 mW/cm^2 using a calibrated Si solar cell (from ReRa Solutions). Capacitance–voltage (C–V) measurements of the finished device were made in the dark using an Agilent E4980A Precision LCR Meter operating at 500 kHz frequency and 100 mV step with bias voltage from 0 to −1 V.

3. Results and discussion

The top-view SEM image of a representative thin film selenized under a selenium pressure of 140 mbar shown in Fig. 1(a) reveals the CZTSSe thin film is composed of densely packed micron-sized grains. However, with a low selenium pressure down to 31 or 53 mbar, discontinuous films with isolated small grains are observed in the thin film after selenization (see Fig. S1 in the online supplementary data at http://stacks.iop.org/JJAP/57/00XX00/mmedia). Therefore, only CZTSSe thin film obtained at selenium pressures of 75, 140, and 226 mbar were considered for solar cell devices. Figure 1(b) shows the XRD patterns of the CZTSSe thin films selenized at different selenium vapor pressures. The intensity ratio of diffraction peaks (112) to (220) increased 5 times when the Se pressure increased from 75 to 226 mbar. This indicates that higher Se pressure facilitates crystal growth along the (112) direction. The thickest large grain (LG) layer of 880 nm was obtained at a high selenium pressure of 226 mbar. A more detailed discussion of the film thickness is presented later in the depth profile analysis. Based on the shift of the (112) peak, the Se/(Se + S) ratio in the thin film was calculated to be 0.89, 0.94, and 0.97 when selenium vapor pressure was 75, 140, and 226 mbar, respectively. Two peaks belonging to Mo(Se,S)$_2$ are also observable around 32 and 56°. In contrast to the signal increase of CZTSSe, it is interesting to find that the signal intensity of the Mo(Se,S)$_2$ peaks is decreasing at higher selenium vapor pressure. This indicates thinner Mo(Se,S)$_2$ layers are formed under higher selenium vapor pressure. Note that the peak at 24.5° is an experimental artefact due to insufficient Ni-filtering in the diffractometer.

(a)

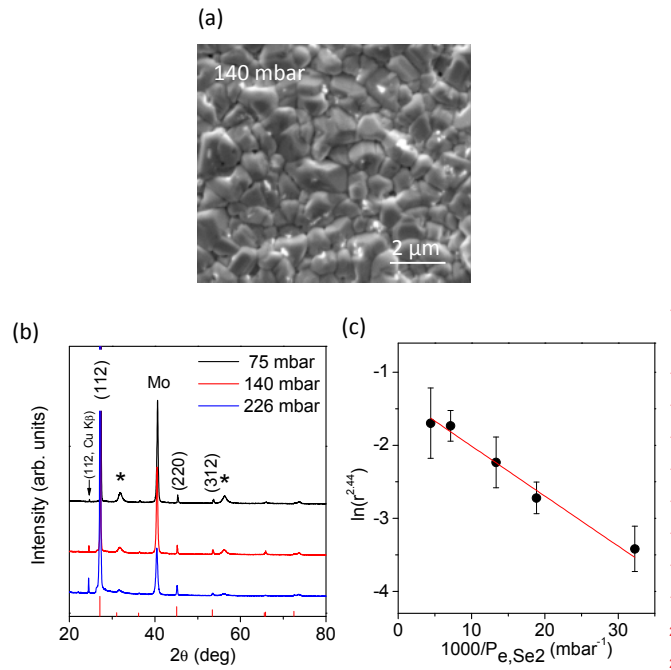

(b)   (c)

Fig. 1. (Color online) (a) Top view SEM image of the CZTSSe thin film selenized at selenium vapor pressure of 140 mbar. Note that the white particles observed on the surface are a consequence of charging during the electron microscopy rather than a secondary phase. (b) XRD patterns of thin film selenized at different selenium vapor pressures. The distinct peaks match well with the reference pattern of CZTSe (PDF 052-0868) given at the bottom. The peaks marked by the asterisks belong to Mo(Se,S)$_2$. (c) Variation of average CZTSSe grain size as a function of selenium vapor pressure.

We have previously demonstrated that CZTSSe follows a normal grain growth with a grain growth exponent of $n = 2.44$.[16]

$$r^n - r_0^n = Kt = K_0 t \exp\left(-\frac{Q}{RT}\right), \qquad (3)$$

where r_0 and r are the average grain radius before and after selenization, respectively, K_0 is the pre-exponential constant, t is the time, Q is the activation energy for grain boundary motion (kJ/mol), R is the gas constant (8.31 J mol^{-1} K^{-1}), and T is the selenization temperature (K). The normal grain growth model can be further developed into a pressure dependent function:

$$r^n - r_0^n = K_0 t \exp\left(-\frac{Qn_{Se_2}}{V_b P_{e,Se_2}}\right), \qquad (4)$$

where V_b is the graphite box volume, and n_{Se_2} is the number of Se moles in the vapor phase. A plot of $\ln r^{2.44}$ as a function of $1000/P_{e,Se_2}$ is shown in Fig. 1(c) where the linear fit confirms the applicability of the normal grain growth model.

The SIMS depth profiles of a CZTSSe thin film selenized at selenium vapor pressure of 140 mbar is shown in Fig. 2(a). Except at the very surface of the thin film where oxygen increases the yield of positive ions, the metal constituent elements of CZTSSe exhibit uniform distribution until ~700 nm where a C signal attributable to the long chain ligand used in the fabrication, begins to increase. Additionally, the significant increase of Mo signal indicates the start of the CZTSSe/Mo interface. Based on the curves of Mo and C, the spectra can be divided into four compositional zones
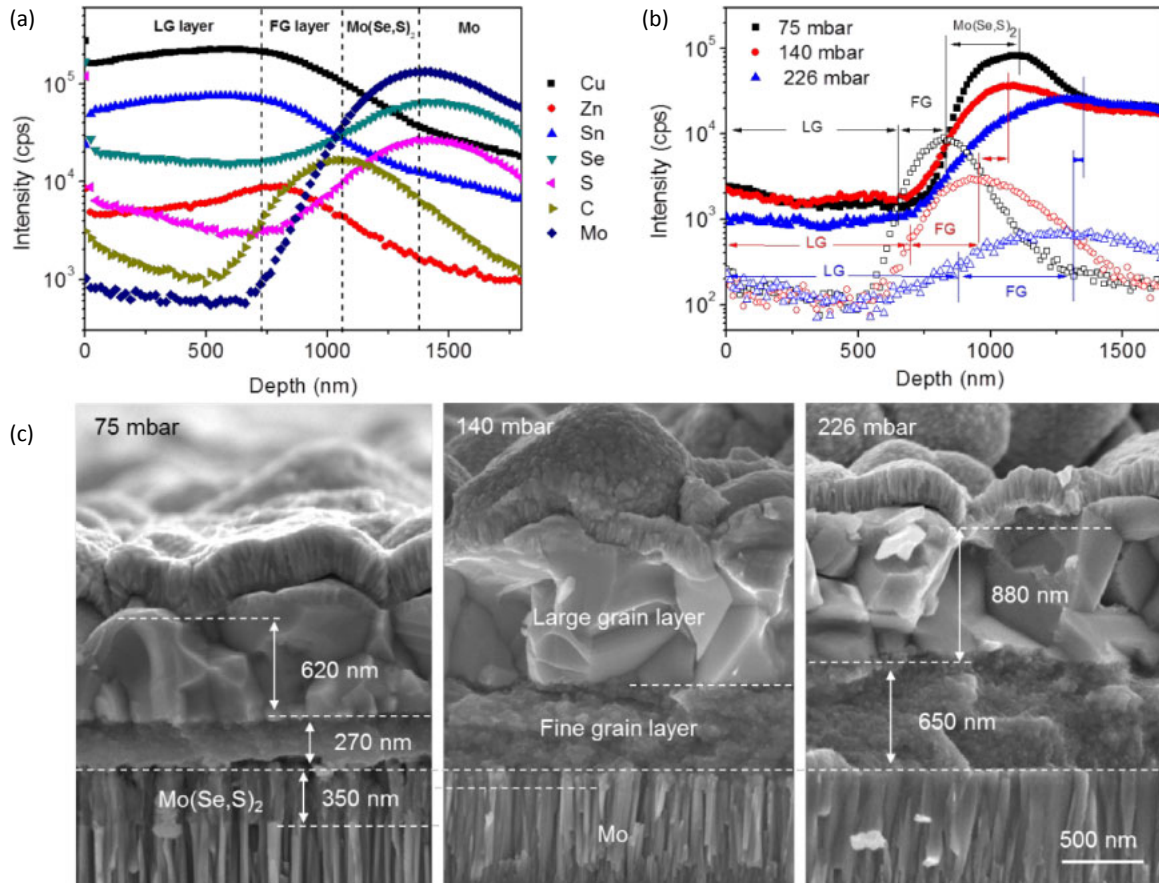
JJAP PROOF

Fig. 2. (Color online) (a) SIMS depth profiles of a CZTSSe film selenized at selenium vapor pressure of 140 mbar. The dashed vertical lines divide the profile into four composition zones. (b) Mo and C distributions through the CZTSSe films selenized at different selenium vapor pressures. The closed symbols represent Mo signals at different selenium vapor pressures while open symbols represent C signals. (c) Cross-sectional SEM image of CZTSSe thin film solar cells selenized at different selenium vapor pressures. The scale bar of 500 nm applies to all images.

marked by the vertical lines. A LG layer composed of high purity CZTSSe with low carbon content is formed above a fine grain (FG) layer that is found before the C signal peaks. The FG layer is rich in carbon, especially close to the substrate interface as C is driven towards the back of the absorber layer upon the selenization. Below the FG layer, a $Mo(Se,S)_2$ layer is found in the region between the C and Mo signal peaks where high levels of Se and S signals exist between the CZTSSe film and Mo substrate.

The different layers in CZTSSe thin films therefore can be determined by using the Mo and C signals as demonstrated in Fig. 2(b). The LG layer starts at the film surface and extends to the C signal half peak height. The FG layer is then formed from the C signal half peak to the peak before a $Mo(Se,S)_2$ layer is formed between the C signal peak and Mo signal peak. It is clear that the LG layer and FG layer both become thicker as selenium vapor pressure increases. However, the $Mo(Se,S)_2$ layer becomes thinner and can hardly be determined under a selenium vapor pressure of 226 mbar. Representative cross-sectional SEM images of complete PV devices at different selenium vapor pressures are given in Fig. 2(c) to study the CZTSSe structure and morphology directly. At a selenium pressure of 75 mbar, the cross-sectional image of the selenized thin film reveals the four-layer structure identified from the SIMS data. From the bottom is the Mo substrate with a columnar grain structure, a $Mo(Se,S)_2$ layer, a carbon rich residual FG layer, and a

carbon free LG layer. As shown in Fig. 2(c), higher selenium vapor pressure facilitates growth of LG layer, however the FG layer now occupies a larger fraction of the total CZTSSe absorber layer thickness. For example, this increases from 0.30 at 75 mbar to 0.42 at 226 mbar. In addition and consistent with the SIMS and XRD characterizations, the $Mo(Se,S)_2$ layer is too thin to be observed at 226 mbar. The involvement of carbon, via the long chain ligand oleylamine is expected to be the main cause of this unique bilayer morphology exhibited in Fig. 2(c) as no such bottom FG layers are obtained in carbon free techniques.[20–22] The small network of grain boundaries in the FG layer may contribute high series resistance and reduce the fill factor of solar cells.[11,23,24]

It is difficult to draw conclusions about the total thickness of the entire film due to the combination of uncertainty in the precursor thickness (nominally $1.0 \pm 0.1 \mu m$) and surface roughness however, it can be clearly seen that as the thickness of the FG layer increases, the $MoSe_2$ layer becomes thinner. This is somewhat surprising as other works report an increase in the thickness of $MoSe_2$ with increasing selenization pressure.[25] We propose that the presence of the FG layer acts as a barrier, potentially through the formation of polymerized CSe_2 compounds which limits the reaction of Mo with Se.[26] This effect becomes more pronounced as the thickness of the FG layer increases resulting in a thinner $MoSe_2$ layer at higher pressure.
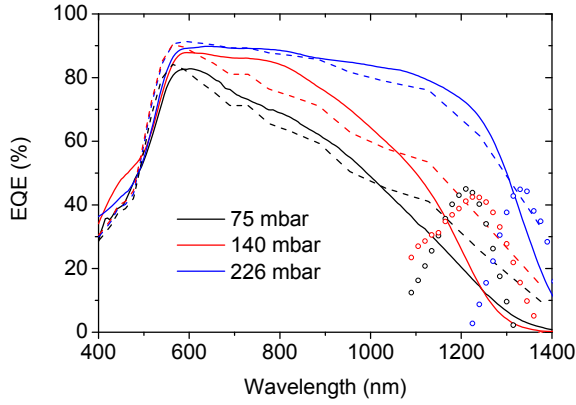
Fig. 3. (Color online) Experimental and reconstructed EQE curves of solar cells fabricated using CZTSSe thin films selenized at different selenium vapor pressures. Solid lines show the experimental data while the dashed lines are based on Eq. (5). Differential EQE data are given by the open circles.

EQE measurements were used to understand the effect of the selenium vapor pressure on the device performance. From the experimental data in Fig. 3, the devices show improved carrier collection efficiency in the visible and near-infrared wavelength ranges when higher selenium vapor pressure was used in the selenization process. In particular, a nearly ideal top-hat shaped EQE characteristic is observed when selenium vapor pressure is increased to 226 mbar. The device made from the absorber annealed at a selenium vapor pressure of 226 mbar reveals a photocurrent efficiency of >85% over a wide wavelength range from 550 to 1050 nm without an antireflection coating.

In order to understand the improvement in the EQE towards long wavelength, the data were modeled using the modified Gärtner equation:[27]

$$\text{EQE} = h' \times \exp(-\alpha_{\text{CdS}} d_{\text{CdS}})$$
$$\times \exp(-\alpha_{\text{ZnO}} d_{\text{ZnO}}) \left[1 - \frac{\exp(-\alpha_{\text{CZTSSe}} W)}{1 + \alpha_{\text{CZTSSe}} L_{\text{eff}}} \right], \quad (5)$$

where h' is the prefactor for interface recombination, α_i are the absorption coefficients of CdS, ZnO, and CZTSSe, and taken from Adachi.[28] d_i are the thicknesses of the CdS and ZnO layer and set to 60 and 35 nm respectively for the modelling. L_{eff} is the effective diffusion length, and W the depletion width given by

$$W = \sqrt{\frac{2 V_{\text{bi}} \varepsilon_r \varepsilon_0}{q N_a}}. \quad (6)$$

Here, V_{bi} is the built-in potential and set to 0.90 V, q the electronic charge, N_a the acceptor concentration, and ε_0 and ε_r ($\varepsilon_r = 14.9$) are the free space and semiconductor permittivities respectively.[28] The EQE curves can hence be generated for different values of h', L_{eff}, and N_a. In this way it was possible to reconstruct EQE curves which qualitatively match the experimental data as shown in Fig. 3. N_a values were obtained from Mott–Schottky plots (see Fig. S2 in the online supplementary data at http://stacks.iop.org/JJAP/57/00XX00/mmedia) and the discrepancy observed at long wavelength is due to the variations in α_{CZTSSe} between the samples where the S/Se varies. In contrast, the modelling is performed using the value of α for the pure selenide case. The corresponding values of h' and L_{eff} derived from this modelling are given in

Table I. The experimental values of doping concentration and calculated values of diffusion length.

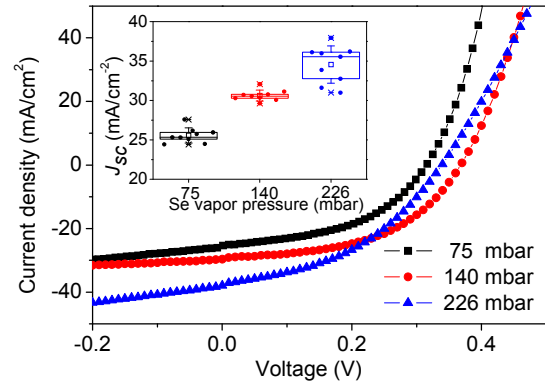|	From simulation		From C–V
$P_{\text{e,Se}_2}$ (mbar)	h' (%)	L_{eff} (nm)	N_a (cm^{-3})
75	90.0	147	5.8×10^{16}
140	94.9	294	6.7×10^{16}
226	92.1	1010	2.1×10^{16}

Fig. 4. (Color online) J–V curves of solar cells with CZTSSe thin film absorbers selenized at different vapor pressures. The inset is the J_{sc} distribution of the nine solar cells on each substrate.

Table I. The values of h' are consistent with other work and the small increase with pressure is indicative of a reduction in interface recombination.[27] Large variations in diffusion length are observed where L_{eff} for the device made from the absorber selenized at a selenium vapor pressure of 226 mbar has increased by one order of magnitude to ~1 μm. $L_{\text{eff}} > 1$ μm is consistent with the value reported by Lee for co-evaporated Cu$_2$ZnSnSe$_4$ (CZTSe) however, we stress that the phenomenological nature of the model (which depends on surface roughness and absorption coefficient) gives rise to uncertainty in the result and the obtained value of L_{eff} should be taken as an upper limit.[29] The important point is that the observed increase in the EQE towards long wavelength can be attributed to a significant increase in the minority carrier diffusion length.

J–V curves of the best device at each selenium vapor pressure are shown in Fig. 4 with the device parameters extracted from the J–V curves summarized in Table II.

The best efficiency values for the devices selenized at 75, 140, and 226 mbar are 3.76, 5.41, and 5.38% respectively. A substantial part of this evolution derives from J_{sc} which across all the devices yields average values (see inset to Fig. 4) of 25.57 ± 1.00, 30.62 ± 0.77, and 34.56 ± 2.20 mA/cm^2 at 75, 140, and 226 mbar, respectively (see also Fig. S3 in the online supplementary data at http://stacks.iop.org/JJAP/57/00XX00/mmedia for variations in efficiency, open circuit voltage and fill factor). The values are consistent with the values of J_{sc} obtained by integrating the EQE spectra with the discrepancy accounted for by the contact area. We obtained a champion J_{sc} of 37.9 mA/cm^2 for a device selenized at 226 mbar which to the best of our knowledge is the highest value obtained for CZTSSe solar cells made from CZTS nanoparticle inks.

JJAP PROOF

Table II. Summary of champion photovoltaic parameters as a function of selenization pressure.

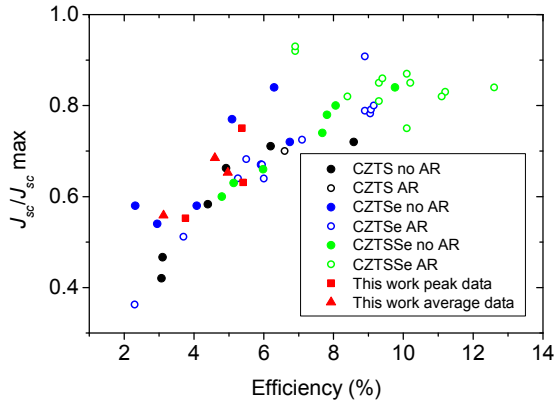| P_{e,Se_2} (mbar)	η (%)	V_{oc} (V)	J_{sc} (mA/cm^2)	J_{sc} (EQE) (mA/cm^2)	FF (%)	R_S ($\Omega \cdot$cm^2)	R_{SH} ($\Omega \cdot$cm^2)	E_g (eV)	$E_g - qV_{oc}$ (eV)
75	3.76	0.31	25.3	28.1	48.3	3.3	40	1.02	0.71
140	5.41	0.36	29.6	32.8	50.7	3.1	77	1.00	0.64
226	5.38	0.33	37.9	39.5	43.0	3.9	26	0.93	0.60

Fig. 5. (Color online) The ratio of J_{sc} to $J_{sc,max}$ as function of solar energy conversion efficiency.

In order to put our result in context, it is also worth considering the ratio of J_{sc} to $J_{sc,max}$ where $J_{sc,max}$ is a theoretical value obtained by integrating the AM1.5 spectrum from 400 nm to the band gap energy E_g. Figure 5 shows this ratio as function of solar energy conversion efficiency for broad range of CZTS, CZTSSe, and CZTSe devices (with and without antireflective coatings) from the literature. Note that a complete list of these data and their references may be found in the Supplementary Information. Importantly, these data demonstrate that high values of J_{sc} are entirely possible for device efficiencies <6%, emphasizing a pressing need for improvements to V_{oc}. Also shown in Fig. 5 are the data from this work and it is clear that our devices agree well with the observed trend obtained from the literature. For additional reference, the Supplementary Information also includes analyses of V_{oc} and fill factor for the works shown in Fig. 5, confirming that the values obtained from our devices are consistent with a broad range of independent works.

The increase in J_{sc} with selenization pressure also correlates with an decrease in the E_g determined from d(EQE)/dE as shown in Table II. The reduction in E_g is attributed to the increased Se incorporation in the film with increasing selenium vapor pressure. From fundamental solar cell theory, the increase in J_{sc} due to the band gap variation is <6 mA/cm^2,[30] however we observe an increase of >12 mA/cm^2 and therefore the improvement in performance cannot be explained by the reduction in E_g alone. The improvement in J_{sc} towards higher vapor pressures is accompanied by a decrease in V_{oc} which limits the overall device efficiency. Despite this drop, Table II indicates that the V_{oc} deficit relative to the energy band gap is actually smallest for a selenium vapor pressure of 226 mbar. However, the efficiency is reduced by a lower fill factor (FF) via shunt (R_{SH}) and series (R_S) resistances which are likely to result from a thicker fine grain layer and quasi-absence of Mo(Se,S)$_2$.[11,23,31] The selenization optimization here thus

represents an avenue to improve the device performance of CZTSSe solar cells by boosting J_{sc} and narrowing the V_{oc} deficit simultaneously. The challenge for further investigation is to preserve these advantages while simultaneously achieving a high fill factor.

4. Conclusions

High quality CZTSSe photovoltaic absorber layers were fabricated by selenizing the as-deposited thin film made from CZTS nanoparticle inks. Increasing the selenium vapor pressure resulted in larger CZTSSe grains. Solar cells made from these absorbers showed broad spectrum external quantum efficiency which crucially, demonstrated significant enhancement towards long wavelength. This was explained by a substantial increase in the minority carrier diffusion length resulting in high values of short circuit current density. The overall device efficiency was offset by a slight reduction in the open circuit voltage and increased series resistance attributable to a fine grain sub-layer that is characteristic of the nanoparticle ink fabrication method. Despite the reduction in open circuit voltage, the deficit to the energy band gap was also minimized at the highest selenium vapor further demonstrating considerable potential for the technology.

1) F. Luckert, D. I. Hamilton, M. V. Yakushev, N. S. Beattie, G. Zoppi, M. Moynihan, I. Forbes, A. V. Karotki, A. V. Mudryi, M. Grossberg, J. Krustok, and R. W. Martin, Appl. Phys. Lett. **99**, 062104 (2011).
2) A. Polman, M. Knight, E. C. Garnett, B. Ehrler, and W. C. Sinke, Science **352**, aad4424 (2016).
3) I. Repins, C. Beall, N. Vora, C. DeHart, D. Kuciauskas, P. Dippo, B. To, J. Mann, W. C. Hsu, A. Goodrich, and R. Noufi, Sol. Energy Mater. Sol. Cells **101**, 154 (2012).
4) A. V. Moholkar, S. S. Shinde, A. R. Babar, K. U. Sim, H. K. Lee, K. Y. Rajpure, P. S. Patil, C. H. Bhosale, and J. H. Kim, J. Alloys Compd. **509**, 7439 (2011).
5) S. G. Haass, M. Diethelm, M. Werner, B. Bissig, Y. E. Romanyuk, and A. N. Tiwari, Adv. Energy Mater. **5**, 1500712 (2015).
6) S. Ahmed, K. B. Reuter, O. Gunawan, L. Guo, L. T. Romankiw, and H. Deligianni, Adv. Energy Mater. **2**, 253 (2012).
7) C. K. Miskin, W. C. Yang, C. J. Hages, N. J. Carter, C. S. Joglekar, E. A. Stach, and R. Agrawal, Prog. Photovoltaics **23**, 654 (2015).
8) G. Zoppi, I. Forbes, R. W. Miles, P. J. Dale, J. J. Scragg, and L. M. Peter, Prog. Photovoltaics **17**, 315 (2009).
9) T. K. Todorov, K. B. Reuter, and D. B. Mitzi, Adv. Mater. **22**, E156 (2010).
10) W. Wang, M. T. Winkler, O. Gunawan, T. Gokmen, T. K. Todorov, Y. Zhu, and D. B. Mitzi, Adv. Energy Mater. **4**, 1301465 (2014).
11) H. Zhou, W. C. Hsu, H. S. Duan, B. Bob, W. Yang, T. B. Song, C. J. Hsu, and Y. Yang, Energy Environ. Sci. **6**, 2822 (2013).
12) T. J. Huang, X. Yin, C. Tang, G. Qi, and H. Gong, J. Mater. Chem. A **3**,

17788 (2015).

13) C. J. Hages, M. J. Koeper, C. K. Miskin, K. W. Brew, and R. Agrawal, Chem. Mater. **28**, 7703 (2016).

14) Q. Guo, J. V. Caspar, K. E. Roelofs, S. Subramoney, and H. D. Rosenfeld, Chem. Mater. **26**, 5664 (2014).

15) Y. Cao, M. S. Denny, J. V. Caspar, W. E. Farneth, Q. Guo, A. S. Ionkin, L. K. Johnson, M. Lu, I. Malajovich, D. Radu, H. D. Rosenfeld, K. R. Choudhury, and W. Wu, J. Am. Chem. Soc. **134**, 15644 (2012).

16) Y. Qu, G. Zoppi, and N. S. Beattie, Sol. Energy Mater. Sol. Cells **158**, 130 (2016).

17) Y. Qu, G. Zoppi, R. W. Miles, and N. S. Beattie, Mater. Res. Express **1**, 045040 (2014).

18) Y. Qu, G. Zoppi, and N. S. Beattie, Prog. Photovoltaics **24**, 836 (2016).

19) J. J. Scragg, Dr. Thesis, Department of Chemistry, University of Bath, Bath (2010).

20) J. Zhong, Z. Xia, C. Zhang, B. Li, X. Liu, Y. B. Cheng, and J. Tang, Chem. Mater. **26**, 3573 (2014).

21) T. J. Huang, X. Yin, C. Tang, G. Qi, and H. Gong, ChemSusChem **9**, 1032 (2016).

22) S. Giraldo, E. Saucedo, M. Neuschitzer, F. Oliva, M. Placidi, X. Alcobe, V. Izquierdo-Roca, S. Kim, H. Tampo, H. Shibata, A. Perez-Rodriguez, and P. Pistor, Energy Environ. Sci. (in process) [DOI: 10.1039/C7EE02318A].

23) H. Zhou, T. B. Song, W. C. Hsu, S. Luo, S. Ye, H. S. Duan, C. J. Hsu, W. Yang, and Y. Yang, J. Am. Chem. Soc. **135**, 15998 (2013).

24) S. G. Haass, C. Andres, R. Figi, C. Schreiner, M. Bürki, Y. E. Romanyuk, and A. N. Tiwari, Adv. Energy Mater. **8**, 1701760 (2018).

25) X. Liu, Y. Feng, H. Cui, F. Liu, X. Hao, G. Conibeer, D. B. Mitzi, and M. Green, Prog. Photovoltaics **24**, 879 (2016).

26) B. D. Chernomordik, P. M. Ketkar, A. K. Hunter, A. E. Béland, D. D. Deng, and E. S. Aydil, Chem. Mater. **28**, 1266 (2016).

27) J. de Wild, E. Kalesaki, E. V. C. Robert, and P. J. Dale, IEEE J. Photovoltaics **7**, 268 (2017).

28) S. Adachi, in *Copper Zinc Tin Sulfide-Based Thin Film Solar Cells*, ed. K. Ito (Wiley, Chichester, U.K., 2015) p. 149.

29) Y. S. Lee, T. Gershon, O. Gunawan, T. K. Todorov, T. Gokmen, Y. Virgus, and S. Guha, Adv. Energy Mater. **5**, 1401372 (2015).

30) F. Meillaud, A. Shah, C. Droz, E. Vallat-Sauvain, and C. Miazza, Sol. Energy Mater. Sol. Cells **90**, 2952 (2006).

31) S. Lopez-Marino, M. Espíndola-Rodríguez, Y. Sánchez, X. Alcobé, F. Oliva, H. Xie, M. Neuschitzer, S. Giraldo, M. Placidi, R. Caballero, V. Izquierdo-Roca, A. Pérez-Rodríguez, and E. Saucedo, Nano Energy **26**, 708 (2016).